energies

MDPI

Article

Research on High-Frequency Modification Method of Industrial-Frequency Smelting Transformer Based on Parallel Connection of Multiple Windings

Huiqin Zhou [1], Xiaobin Yu [2], Wei Xu [3] and Weibo Li [3,4,*]

[1] College of Electric Power, Yinchuan Energy Institute, Yinchuan 750100, China; 13948927271@163.com
[2] Ningxia Zhongcheng Tebian Technology Co., Ltd., Yinchuan 750100, China; 13519574644@163.com
[3] School of Automation, Wuhan University of Technology, Wuhan 430070, China; 283861@whut.edu.cn
[4] College of Electrical Engineering, Northwest Minzu University, Lanzhou 730124, China
* Correspondence: liweibo@whut.edu.cn

Abstract

Under the background of "dual-carbon" strategy and global energy transition, the metallurgical industry, which accounts for 15–20% of industrial energy consumption, urgently needs to reduce the energy consumption and emission of DC power supply of electric furnaces. Aiming at the existing 400–800 V/≥3000 A industrial-frequency transformer-rectifier system with low efficiency, large volume, heat dissipation difficulties and other bottlenecks, this thesis proposes and realizes a high-frequency integrated DC power supply scheme for high-power electric furnaces: high-frequency transformer core and rectifier circuit are deeply integrated, which breaks through and reduces the volume of the system by more than 40%, and significantly reduces the iron consumption; multiple cores and three windings in parallel are used for the system. The topology of multiple cores and three windings in parallel enables several independent secondary stages to share the large current of 3000 A level uniformly, eliminating the local overheating and current imbalance; the combination of high-frequency rectification and phase-shift control strategy enhances the input power factor to more than 0.95 and cuts down the grid-side harmonics remarkably. The authors have completed the design of 100 kW prototype, magneto-electric joint simulation, thermal structure coupling analysis, control algorithm development and field comparison test, and the results show that the program compared with the traditional industrial-frequency system efficiency increased by 12–15%, the system temperature rise reduced by 20 K, electrode voltage increased by 10–15%, the input power of furnace increased by 12%, and the harmonic index meets the requirements of the traditional industrial-frequency system. The results show that the efficiency of this scheme is 12–15% higher than the traditional IF system, the temperature rise in the system is 20 K lower, the voltage at the electrode end is 10–15% higher, the input power of the furnace is increased by 12%, and the harmonic indexes meet the requirements of GB/T 14549, which verifies the value of the scheme for realizing high efficiency, miniaturization, and reliable DC power supply in metallurgy.

Keywords: smelting equipment; high-frequency transformers; rectifier circuits; high-frequency cores

check for updates

Academic Editors: Federico Barrero and Tek Tjing Lie

Received: 17 June 2025
Revised: 28 July 2025
Accepted: 31 July 2025
Published: 7 August 2025

Citation: Zhou, H.; Yu, X.; Xu, W.; Li, W. Research on High-Frequency Modification Method of Industrial-Frequency Smelting Transformer Based on Parallel Connection of Multiple Windings. *Energies* **2025**, *18*, 4196. https://doi.org/10.3390/en18154196

Copyright: © 2025 by the authors. Licensee MDPI, Basel, Switzerland. This article is an open access article distributed under the terms and conditions of the Creative Commons Attribution (CC BY) license (https://creativecommons.org/licenses/by/4.0/).

1. Introduction

Under the wave of accelerated transformation of the global energy structure and the continuous promotion of the "double carbon" goal (carbon peak and carbon neutral),

the iron and steel, nonferrous, and other metallurgical industries, as typical high-energy-consuming industries, are facing unprecedented pressure on energy conservation and emission reduction [1–3]. Statistics show that the energy consumption of the metallurgical industry accounts for about 15–20% of the global total industrial energy consumption [4], of which the melting process of the electric furnace is particularly prominent. The traditional AC power supply method is difficult to meet the needs of green smelting due to significant line losses and low power factor [5]. Direct current (DC) power supply is becoming an important direction for technological upgrading in the industry due to its higher energy utilization efficiency.

A large number of industrial practices have shown that DC furnaces can save approx. 8–15% compared to AC furnaces for the same capacity and structure [6–9], the main reasons for this being the following:

(1) Elimination of "skin effect" and "neighbor effect" inherent in AC system, line loss is reduced by 7–12%;
(2) Reduced electrode-to-electrode electromagnetic interference, improving system stability by more than 20% [10];
(3) The voltage drop of the lead wire is reduced by 10–15%, and the power density of the furnace is increased by 12–18% [11].

In addition, DC melting offers a combination of 30–40% lower electrode consumption, 15–20 dB lower noise, and 8–10% higher productivity [12]. Thanks to these outstanding performances, the global DC melting equipment market size has been growing rapidly from USD 35 billion in 2023, and is expected to exceed USD 55.2 billion in 2028 [13–15].

Despite the strong market demand, the large-scale application of high-power DC smelting equipment is still limited by the core power supply system technology bottlenecks, mainly reflected in the following:

(1) Industrial-frequency transformer + external rectifier cabinet program efficiency is limited: I.F. transformer iron losses usually account for 40–50% of the total system losses, and the transformer has a large size, occupying an area 50–60% higher than the high-frequency program; rectifier link additional losses further lead to a decline in system efficiency of 3–5% [16–20].
(2) Difficulty in high-current thermal management: When the output current reaches 3000 A, even if the line resistance is only 1 mΩ, it will generate about 9 kW of copper heat loss. Conventional single-channel outputs are prone to localized high temperatures and have to rely on complex forced air or water cooling systems, which increases the cost and maintenance burden [19,21].
(3) Inadequate current equalization and distribution: The common star or delta connection method is prone to uneven branch circuit currents under high current conditions, with deviations of up to 15–20%, which accelerates equipment aging and shortens service life [22].

Aiming at the above problems, this paper proposes a new solution of high-frequency and integrated smelting power supply, with the following core innovations:

High-frequency breakthrough: Adopting a high-frequency magnetic core and high-efficiency rectifier circuit, the operating frequency is increased to more than 13 kHz, the transformer volume is compressed by 40–50%, and the iron loss is reduced by 35–45%, which lays the foundation for miniaturization and high-efficiency of equipment.

High-current equalization: Designing a three-winding parallel topology, proposing a magnetic coupling current equalization algorithm, and optimizing the spatial layout of the windings, the 3000 A output is uniformly distributed among the three windings, and

the current imbalance is controlled to within 3%, which significantly improves the system reliability and lifespan.

Comprehensive validation and economic evaluation: The developed high-frequency triple-winding melting transformer is evaluated in terms of loss mechanism, volume, and economy to provide a theoretical and experimental basis for engineering promotion.

High-power DC smelting systems impose stringent demands on transformer design, including high current output, low total harmonic distortion (THD), compact size, high thermal stability, and high energy efficiency. However, conventional industrial-frequency transformers often suffer from large volume, limited harmonic suppression capability, and high core and copper losses under heavy load conditions. These drawbacks become even more critical in large-scale metallurgical applications, where long-term high-load operation amplifies energy consumption, thermal stress, and equipment aging.

To address these challenges, this study proposes a novel high-frequency rectifier transformer that integrates nanocrystalline magnetic cores with embedded 48-pulse rectification circuitry. A multi-core parallel topology is employed to evenly distribute 3000 A output current across three magnetically decoupled secondary windings, minimizing thermal hotspots and current imbalance. Furthermore, the use of 13 kHz synchronous switching significantly reduces core and copper losses, while the optimized rectifier configuration ensures THD < 5% and a power factor $\geq$ 0.95 without external compensation. These technical approaches comprehensively solve the bottlenecks of conventional designs and demonstrate significant improvements in power density, energy efficiency, and thermal reliability, as validated by simulation.

The rest of thesis is organized as follows: Section 2 establishes the overall scheme of the system and gives the design of key parameters; Section 3 analyzes in depth the electromagnetic–thermal coupling characteristics of the high-frequency three-winding transformer and the equalization mechanism; Section 4 completes the prototype trial and performance test; Section 5 discusses the economic comparison and the application prospects; and Section 6 sums up the whole paper and looks forward to the direction of the subsequent research.

2. Industrial-Frequency Smelting Transformer High-Frequency Transformation Method

The implementation of high-frequency transformation in industrial-frequency smelting transformers necessitates several critical modifications. Primary among these is the selection of core materials possessing superior hysteresis characteristics [23], such as amorphous alloys [24] or nanocrystalline materials [25]. These materials offer significantly reduced hysteresis losses while concurrently enhancing magnetic permeability. To further mitigate high-frequency eddy current losses [26], employing thin laminations and optimizing core geometry are essential strategies for maximizing magnetic field utilization. Concurrently, the integration of high-frequency rectifier circuits utilizing efficient devices like Schottky diodes or MOSFETs [27] substantially improves rectification efficiency and minimizes switching losses. Collectively, these integrated modifications demonstrably enhance the operational efficiency and stability of industrial-frequency smelting transformers operating under high-frequency conditions.

2.1. Characteristics Selection and Optimization of Core Materials

The hysteresis properties of core materials are critical in the design of electromagnetic devices [28], and the selection needs to consider the application requirements, material types, and their electromagnetic properties. A comparison of the core metrics of magnetic core materials is demonstrated in Table 1, which provides key parameters in their elec-

tromagnetic properties by comparing three different types of core materials—silicon steel sheets, amorphous alloys, and nanocrystals. These parameters include saturation magnetic density B_s (T), coercivity H_c (A/m), resistivity ρ ($\mu\Omega \cdot$ cm), and applicable frequency range.

Table 1. Comparison of core metrics for magnetic core materials.

Parameters	Silicon Steel Sheet	Amorphous Alloy	Nanocrystal
Saturation density Bs (T)	2.03	1.56	1.25
Coercivity Hc (A/m)	30–50	1–3	0.5–1.5
Applicable frequency range	<1 kHz	1–50 kHz	10–500 kHz

First, saturation magnetization density is one of the core indicators for evaluating core materials [29]. The saturation magnetization density of silicon steel sheet is 2.03 T, which is significantly higher than that of amorphous alloys (1.56 T), indicating that silicon steel sheet has a significant advantage in application scenarios such as smelting transformers that require high magnetic flux densities. The superiority of silicon steel sheet allows it to remain dominant in traditional power electronics. Secondly, coercivity is an important parameter for assessing the ease with which a magnetic material can maintain its magnetization after removing an external magnetic field. The coercivity of silicon steel sheet ranges 30–50 A/m, while that of amorphous alloys is lower at 1–3 A/m, and that of nanocrystalline materials is in between at 0.5–1.5 A/m. This suggests that amorphous alloys and nanocrystalline materials can achieve better reversibility under weak magnetic field conditions, and are suitable for applications such as high-frequency transformers and resonators, which require rapid changes in magnetic properties. Regarding resistivity, the resistivity of silicon steel sheet is 47 $\mu\Omega \cdot$ cm, significantly lower than that of amorphous alloys (130 $\mu\Omega \cdot$ cm) and nanocrystals (115 $\mu\Omega \cdot$ cm), and the lower resistivity means that silicon steel sheets are able to minimize losses over long periods of time, improving energy efficiency, which is also very important for power systems. Finally, the applicable frequency range is also an important evaluation dimension for all types of magnetic materials. In applicable frequencies, silicon steel sheets range from <1 kHz, while amorphous alloys and nanocrystalline materials can handle higher frequency signals, the former from 1 to 50 kHz and the latter as high as 10 to 500 kHz. This frequency adaptability makes amorphous alloys and nanocrystalline materials suitable for miniaturized, high-efficiency, high-frequency applications such as switching power supplies and high-frequency converters. Taken together, silicon steel sheets still perform well in traditional low-frequency applications and are suitable for applications with high requirements for magnetic density and resistivity. Amorphous alloys and nanocrystalline materials, on the other hand, are suitable for applications requiring high-frequency operation in electronic devices due to their good high-frequency performance and low coercivity.

Reducing the hysteresis loss power density is of great significance to prolong the service life of the equipment and energy saving and emission reduction, and the hysteresis loss optimization methods include the following two kinds: the first one adopts the field annealing process which can make the amorphous alloy hysteresis loss power density P_h reduce, and the second one can generate the ultrafine grains of less than 50 nm by adding the Cu/Nb in the nanocrystalline cores, so as to make the eddy current loss P_e accounted for the reduced ratio.

Treatment of amorphous alloys using the field annealing process can significantly reduce their hysteresis loss power density, specifically by up to 40%. This process improves the magnetic properties of amorphous materials by heating them in a magnetic field to optimize their internal microstructure. The improved material hysteresis loss energy

conversion efficiency is significantly increased, leading to a reduction in power density, which is expressed as P_h:

$$P_h = k_h f B_m^{\alpha} \quad (1)$$

where the loss power density P_h indicates the energy loss per unit volume of magnetic core in the alternating magnetic field due to the flip of magnetic domains (W/kg), P_h = 3.8 W/kg for amorphous alloys and 1.2 W/kg for nanocrystalline ones; k_h indicates the hysteresis loss coefficient, and studies have shown that the smaller the intrinsic characteristic of the material coercivity H_c is, the lower the k_h is, and the transverse magnetic field annealing in the heat treatment process can make k_h decrease by 30–50%. Table 2 shows the typical values of k_h for typical materials. B_m indicates the peak value of magnetic flux density (T) when the core is in operation, which is usually taken as 0.6–0.8 times the saturation density B_s, and the typical operating point of amorphous alloys is 0.3–0.5 T; α indicates the sensitivity of the hysteresis loss to the change in the density, and is taken as 1.6–2.0 T for conventional materials based on the empirical values from Steinmetz, and 1.4–1.7 T for optimized amorphous alloys.

Table 2. Typical values of hysteresis loss coefficient k_h for typical materials.

Material Type	k_h Range (SI Units)	Test Condition
Silicon steel sheet	0.15–0.25	50 Hz, 1.5 T
Amorphous alloy	0.05–0.12	10 kHz, 0.3 T
Nanocrystal	0.02–0.06	20 kHz, 0.2 T

The fabrication process of nanocrystalline cores can be effectively achieved by adding elements such as copper and niobium to achieve the formation of ultrafine grains, which can have a grain size of less than 50 nm [30]. This optimization of the microstructure not only improves the magnetic properties of the material but also significantly reduces the eddy current losses. Eddy current loss is the energy loss due to the eddy currents formed in the material by the current induced by the alternating magnetic field, and the eddy current loss P_e is expressed as follows:

$$P_e = \frac{(\pi f B_m d)^2}{6\rho} \quad (2)$$

where P_e denotes eddy current loss (W), d denotes crystal size (mm), and f denotes power supply operating frequency (Hz).

The eddy current loss P_e expression provides a quantitative analysis of eddy current loss by taking into account a variety of factors such as material conductivity, frequency, and grain size. By controlling the size of the grains, especially in the nanoscale range, the eddy current paths can be significantly reduced, thereby suppressing eddy current formation and thus achieving lower energy losses.

Table 3 demonstrates typical values of resistivity ρ for different core materials, specifically silicon steel sheet, amorphous alloys, and nanocrystalline materials. These data are important for optimizing the design and performance of electromagnetic devices. In electromagnetic devices, the material resistivity ρ directly affects their efficiency, losses, and overall performance.

Table 3. Typical values of resistivity ρ for different core materials.

Material Type	ρ (μΩ·cm)
Silicon steel sheet	47
Amorphous alloy	130
Nanocrystal	115

Silicon steel sheets have a resistivity of 47 μΩ · cm, and their relatively low resistivity makes them widely used in traditional smelting transformer applications. In smelting transformer design, lower losses mean higher energy conversion efficiency, which can effectively reduce heat generation and extend equipment life. In addition, the magnetic permeability of silicon steel sheet is higher, which is conducive to enhancing the magnetic field strength of the equipment, thus optimizing the working performance of the equipment. Amorphous alloys have a resistivity of 130 μΩ · cm, which is significantly higher than that of silicon steel sheets. This material usually has excellent magnetic properties and a low giant magnetoresistance effect. Despite their relatively high resistivity, amorphous alloys' low loss characteristics make them excellent for high-frequency applications, making them suitable for devices such as high-frequency transformers and inductors. Nanocrystalline materials have a resistivity of 115 μΩ · cm, close to that of amorphous alloys. This material optimizes the magnetic properties of the material with its nanoscale grain structure, typically exhibiting lower magnetic losses and better temperature stability. Nanocrystalline materials show good promise for research and industrial applications, especially in high-performance transformers and electric motors. Their low loss characteristics contribute to increased energy efficiency and reduced operating costs.

2.2. Smelting Transformer High-Frequency Eddy Current Loss Suppression

High-frequency eddy current loss [31] is one of the important factors affecting the performance of amorphous alloy materials. In high-frequency applications, the increase in eddy current loss is mainly due to the energy loss generated by eddy currents in the material. To effectively suppress the high-frequency eddy current loss, it is necessary to pay attention to the skinning depth of the material; in the conductor, the density of the alternating current is gradually weakened by the depth, and the skinning depth δ of an amorphous alloy strip is expressed as follows:

$$\delta = \sqrt{\frac{2\rho}{\omega\mu}} \tag{3}$$

where ω denotes power supply operating frequency (rad/s); μ denotes magnetic permeability (H/m). The optimized expression for the skinning depth takes into account a number of factors such as the conductivity, frequency, and magnetic permeability of the material. By increasing the conductivity of the amorphous alloy or adjusting its magnetic properties, the skinning depth can be effectively reduced, thus reducing the high-frequency eddy current loss. Under the action of high-frequency signals, the current is mainly concentrated in the region near the surface of the material, reducing the formation and propagation of eddy currents within the material. By optimizing the skinning depth, the amorphous alloy material can maintain a lower loss level under high-frequency operation, improving its overall energy efficiency. This optimization not only improves the performance of amorphous materials in transformers, induction heating, and other high-frequency applications, but also extends their service life, making them more practical.

Engineering practice has shown that the effective permeability can be increased by 20% to 40% by transverse magnetic field annealing, thus reducing the skinning depth δ. When designing a 13 kHz amorphous alloy core, the skinning depth δ is calculated as follows:

$$\delta = \sqrt{\frac{2 \times 1.30 \times 10^{-6}}{8.17 \times 10^{4} \times 3.77 \times 10^{-3}}} \approx 25\ \mu\text{m} \tag{4}$$

In the selection process of the material, it is calculated and recommended to select an amorphous material with a thickness of not more than 25 ms. Further, if a material with a

thickness of 18 ms is selected, the eddy current loss is expected to be further reduced by 15% compared to a thickness of 25 ms. This reduction is mainly because thinner materials can reduce the generation of eddy currents under high-frequency conditions, because the formation of eddy currents is affected by the skin depth, and thinner structures can effectively limit the path of eddy currents and reduce eddy current losses.

To gain a deeper understanding of this phenomenon, a more detailed mathematical description and quantitative relationship are provided for Equation (4). This Equation involves several key parameters such as the material's magnetic permeability, electrical conductivity, frequency, and material thickness. The coupling relationships between these parameters are summarized in Table 4.

Table 4. Coupling between key parameters.

Parameter Variation	Effect on Skinning Depth	Engineering Response
Elevated frequency f	$\delta \propto \frac{1}{\sqrt{f}} \rightarrow$ decrease	Use of thinner materials or multi-layer insulation laminations
Resistivity ρ increase	$\delta \propto \sqrt{\rho} \rightarrow$ increase	Thickness requirements can be relaxed to reduce costs
Reduced μ permeability	$\delta \propto \frac{1}{\sqrt{\mu}} \rightarrow$ increase	Core size and losses need to be weighed

Multi-layer core structure design reduces eddy current loss by 30%~50% when material thickness d $\leq \delta$. The typical value of amorphous alloy at 13 kHz is calculated to be 25 μm only. The core splitting technique with a distributed air gap structure is adopted to split a single core into 4 sub-cores with an air gap length l_g of

$$l_g = \frac{\mu_0 N^2 A_e}{L} - \frac{l_e}{\mu_r} \quad (5)$$

where l_g represents the air gap length in mm, with amorphous alloy distributed multi-air gap core value of 0.1~0.5 mm and nanocrystalline core value of 0.05~0.2 mm; μ_0 represents the vacuum permeability, with the standard reference value of $4\pi \times 10^{-7}$ H/m; N stands for the number of turns, with high-frequency transformer turns significantly reduced; A_e indicates the effective cross-sectional area of the magnetic core in m^2; L indicates the target inductance, and the primary inductance of the 80 kVA/13 kHz transformer is approximated to be 500 μH; μ_r indicates the relative permeability, and Table 5 indicates the values of the relative permeability of the amorphous alloys and nanocrystalline materials.

Table 5. Relative permeability values of amorphous alloys and nanocrystalline materials.

Material Type	Initial μ_r	Operating μ_r (13 kHz)
amorphous alloy	5×10^4~1×10^5	2000~5000
nanocrystal	1×10^5~5×10^5	3000~8000

Analyzing Table 5, it is learned that the relative permeability decreases at high-frequency conditions, which is mainly due to the eddy current effect. At high frequencies, alternating currents generate eddy currents in the conductor, which leads to a localized enhancement of the magnetic field and a corresponding decrease in permeability. This phenomenon has important implications for the design and performance evaluation of transformers in high-frequency applications. Combined with Equation (5), further understanding of the interrelationships between relative permeability, air gap, flux density, and other parameters under high-frequency operation is shown in Table 6.

Table 6. Coupling between relative permeability, air gap, and flux density parameters.

Parameter Variation	The Effect on the Air Gap Length l_g	Physical Mechanism
Increase in the number of turns N	$l_g \propto N_2 \rightarrow$ increase	Need more air gap to prevent saturation
Magnetic permeability μ_r increase	l_g decrease	Increased magnetic conductivity of the core itself
Inductance L demand increases	l_g decrease	Higher magnetic energy storage density required

Table 7 demonstrates the measured loss data for different core materials at high-frequency conditions. The total loss of conventional silicon steel is 12.5 W/kg, and the eddy current loss accounts for as much as 68%, indicating that it exhibits significant energy loss in high-frequency operations, which is mainly affected by the eddy current effect. In comparison, the total loss of the amorphous alloy is reduced to 3.8 W/kg, and the percentage of eddy current loss is also reduced to 22%, which shows its superior electromagnetic performance in high-frequency applications and can effectively suppress dynamic energy loss. Nanocrystalline materials show the best performance, with a total loss of only 2.1 W/kg and eddy current losses of only 15%. This result signifies the potential application of nanocrystalline materials in high-frequency transformers, as they not only reduce energy consumption, but also improve overall operational efficiency.

Table 7. Measured loss data of different core materials under high-frequency conditions.

Core Type	Total Loss (W/kg)	Eddy Current Loss as a Percentage
Conventional silicon steel	12.5	68%
Optimization of amorphous alloys	3.8	22%
Nanocrystal	2.1	15%

Figure 1 represents the flow chart of optimized core selection for the high-frequency transformation of a smelting transformer. Figure 1 systematically illustrates the decision pathway for selecting the optimal core material in the high-frequency transformation of smelting transformers. Firstly, the application scenarios are classified into two categories of frequency greater than 10 kHz and frequency less than 10 kHz through the determination of frequency demand, where the former is suitable for the selection of amorphous or nanocrystalline materials, and the latter is recommended to be used with silicon steel sheet. At the power class discrimination stage, for applications with power less than 50 kW, nanocrystalline cores are recommended to reduce losses and increase efficiency, while for power more than 50 kW, amorphous alloy cores with good resistance to saturation and lower core losses are recommended. Finally, thickness selection is further subdivided according to frequency requirements, with 25 materials being recommended for applications from f = 10 to 20 kHz, and 18 materials being recommended for frequencies above 20 kHz, to effectively reduce eddy current losses and optimize overall transformer performance.

2.3. Industrial-Frequency Smelting Transformer High-Frequency Rectifier Circuit Design

The pulse rectifier bridge constitutes a critical component for alternating current (AC) to direct current (DC) power conversion. In this thesis, a parallel configuration of two six-pulse rectifier bridges is implemented. This topology enhances the current-carrying capability of the rectifier system while simultaneously reducing the output DC voltage ripple. A phase-shifting transformer facilitates a 30° interphase displacement between the bridges: the primary winding employs a star/star (Y/Y) connection to deliver

a 0° phase reference voltage, while the secondary winding utilizes a star/delta (Y/Δ) connection to produce a 30° phase-shifted output. This design not only ensures balanced load distribution across both rectifier sets but also significantly attenuates harmonic content, thereby enhancing the overall power quality of the system.

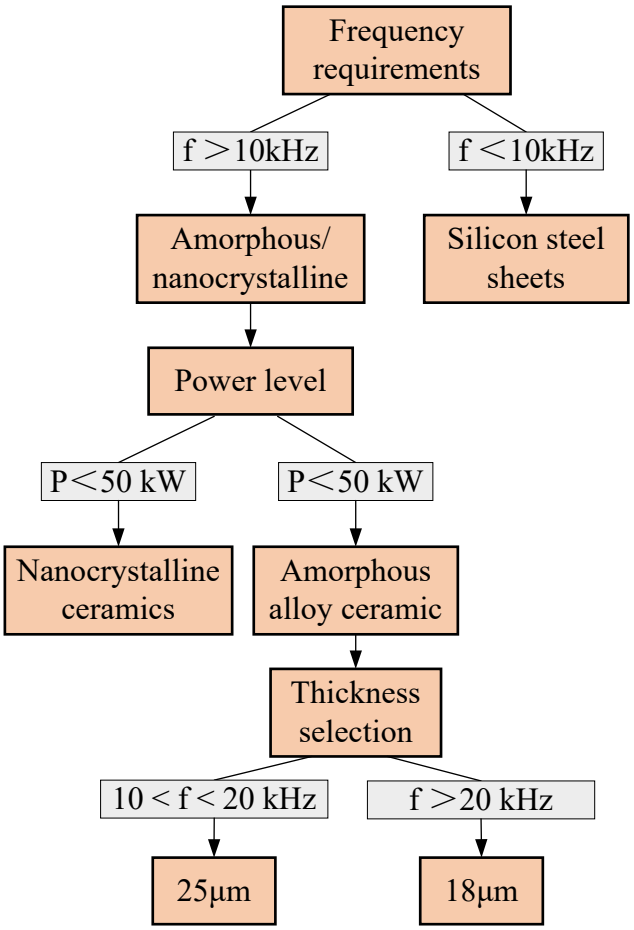


Figure 1. Smelting transformer high-frequency transformation core optimization selection flow chart.

In the selection of the rectification method, the six-pulse wave design has more advantages compared to the traditional three-pulse wave rectification, and the waveform of its output voltage is closer to the ideal DC, which reduces the occurrence of ripple voltage. The output voltage ripple factor γ is calculated as in Equation (6):

$$\gamma = \frac{V_{\text{ripple}}}{V_{\text{dc}}} \tag{6}$$

where V_{ripple} denotes the ripple voltage (V); V_{dc} denotes the rectified output voltage (V). The six-pulse rectifier bridge can utilize the transformer's capacity more efficiently, reducing system losses and heat generation and improving overall operating efficiency.

3. Three-Winding Parallel Shunt Topology Optimization Approach

3.1. Three-Winding Parallel Shunt Magnetic Coupling Equilibrium Modeling

The Three-Winding Parallel Shunt Magnetic Coupling Equilibrium (TPMCE) model serves as an electromagnetic design framework for optimizing three-winding transformer performance. This model enables three windings to be independently loaded while achieving current balancing through magnetic coupling. The TPMCE model provides a scientific and quantitative foundation for modern power systems, ensuring efficient power transfer

and balanced load distribution under high-current conditions. The mutual inductance relationships governing the windings are described by the following equations:

$$\begin{cases} V_1 = j\omega(L_1 I_1 + M_{12} I_2 + M_{13} I_3) \\ V_2 = j\omega(M_{21} I_1 + L_2 I_2 + M_{23} I_3) \\ V_3 = j\omega(M_{31} I_1 + M_{32} I_2 + L_3 I_3) \end{cases} \tag{7}$$

where L_{i} (i = 1,2,3) denotes the triple winding self-inductance (H); M_{12} and M_{13} denote the mutual inductance (H) between winding 1 and windings 2 and 3; M_{21} and M_{23} indicate the mutual inductance (H) between winding 2 and windings 1 and 3; M_{31} and M_{32} denote the mutual inductance (H) between winding 3 and windings 1 and 2; I_{i} (i = 1,2,3) indicates the current (A) flowing through the three windings; V_{i} (i = 1,2,3) indicates (A); and ω denotes angular frequency and $\omega = 2\pi f$ (rad/s).

The equation for the equilibrium condition is as follows:

$$M_{ij} = k\sqrt{L_i L_j} \tag{8}$$

where M_{ij} denotes the mutual inductance (H) between winding i and winding j, and k denotes the degree of magnetic coupling between the windings, which usually ranges from 0 to 1.

In the design of a three-winding transformer, an 80 kVA/13 kHz transformer is used as an example, which is designed to have a self-inductance of $L_1 = L_2 = L_3 = 450\mu$H, that is matched to ensure that the electrical characteristics are similar between the windings, thus reducing the energy losses and disturbances caused by imbalance. In addition, 18 turns were used for all three windings, on which the error in the copper cross-section area was controlled within 1%. The importance of self-inductive matching is that it reduces the differences between windings, which in turn reduces the heat generated due to unbalanced currents, thus ensuring safe and stable operation of the transformer under high load conditions.

In mutual inductance optimization, the measured coupling coefficient in this thesis was $k_{12} = k_{23} = k_{13} = 0.97$, and this high coupling coefficient indicates that the magnetic coupling between the windings is good, which effectively improves the energy transfer efficiency of the transformer. The design maintains a fixed winding pitch of 2.5 mm and incorporates a nanocrystalline magnetic shield to mitigate flux leakage and enhance electromagnetic compatibility (EMC). During the design process, a 5% inductance imbalance tolerance (ΔL) was established, representing the permissible variation in self-inductance under fluctuating load conditions. Through precise regulation of self-inductance and mutual inductance parameters, this electromagnetic design methodology provides a quantitative framework for achieving balanced high-current operation. Consequently, the approach significantly enhances the operational efficiency, power delivery stability, and service life of smelting transformers.

3.2. Winding Space Layout Optimization Strategy

In the design of smelting transformers, the optimization of the spatial layout of the windings is an important aspect of performance and efficiency. The optimized winding layout not only significantly reduces electromagnetic losses, but also improves the power density and thermal management of the device. The spatial layout of the windings mainly includes parameters such as winding height, winding thickness, and insulation distance between neighboring windings, and the resonant induction $L_{\sigma i}$ (i = 1,2,3) is expressed as follows:

$$L_{\sigma 1} = L_{\sigma 2} = L_{\sigma 3} = \frac{3\mu_0 N^2 h}{b}\left(\sigma + \frac{a_1 + a_2}{3}\right) \tag{9}$$

where h is the winding height (m); a_1 and a_2 are the spoke thicknesses (m); and σ is the insulation distance (m).

Analysis of Equation (9) reveals that resonant inductive coupling depends not only on structural geometry but also exhibits strong parametric relationships with intra-winding current dynamics and external magnetic field conditions. Optimization of these variables maximizes mutual inductance while minimizing stray losses, thereby achieving dual improvements in power factor correction and load capability for smelting transformers. Implementation of the winding spatial configuration strategy employs finite element analysis (FEA) to simulate electromagnetic field distributions under parametric variations. Comparative evaluation of operational scenarios identifies the optimal winding architecture that maximizes energy conversion efficiency while satisfying structural integrity constraints. This systematic approach is quantitatively validated through the critical design parameters documented in Table 8.

Table 8. Smelting transformer three-winding key technical parameters.

Parameters	Design Value	Implementation Methodology
phase difference	$120^\circ \pm 0.5^\circ$	Laser positioning winding machine
magnetic field inhomogeneity	<3%	Finite element optimization (Maxwell simulation)
axial deviation	$\leq$0.1 mm/m	CNC winding platform

Table 8 enumerates critical design parameters, including phase difference, magnetic field inhomogeneity, and axial deviation. Precise control and optimization of these parameters directly influence transformer efficiency, operational stability, and overall performance.

Firstly, the phase difference design specification is $120^\circ \pm 0.5^\circ$. This parameter ensures optimal phase separation, facilitates effective magnetic field mutual inductance, and enhances energy transfer efficiency. During manufacturing, computerized laser positioning systems enforce strict adherence to this phase tolerance throughout winding fabrication.

Secondly, the magnetic field inhomogeneity is constrained to <3% per the design criteria. This metric critically governs transformer performance and stability. Magnetic field non-uniformity induces eddy current losses, elevates operational temperatures, and excites mechanical vibrations. In extreme scenarios, such inhomogeneity may precipitate equipment failure. Consequently, finite element analysis (FEA) optimization during the design phase enables precise magnetic field distribution computation and enhancement, thereby improving field uniformity.

Thirdly, axial deviation tolerance is specified at <0.1 mm. Computer numerical control (CNC) winding platforms implement high-precision machining to ensure dimensional compliance with design standards during component production. This precision manufacturing not only facilitates assembly but also ensures structural integrity and enhances operational reliability throughout the transformer lifecycle.

4. Performance Evaluation of High-Frequency Three-Winding Smelting Transformers

4.1. Analysis of Loss Mechanism of High-Frequency Three-Winding Smelting Transformer

Transformer losses mainly include core losses and winding losses, i.e., iron and copper losses. The improved Steinmetz equation is used to calculate the core loss P_{Fe} at high frequencies with the mathematical equation:

$$P_{\mathrm{Fe}} = k_h f^{\alpha} B^{\beta} + k_e (fB)^2 \tag{10}$$

where P_{Fe} denotes the core loss (W) and B denotes the magnetic induction (T); k_{h} denotes the hysteresis loss coefficient; k_{e} denotes the eddy current loss coefficient; based on experience [32], it follows that $\alpha \approx 1.5$; $\beta \approx 2.5$; and f denotes the frequency of the AC power supply (Hz).

The expression for the winding loss P_{Cu} after considering the skin effect and neighborhood effect is given by the following:

$$P_{\mathrm{Cu}} = I_{rms}^2 R_{dc}\left[1 + \frac{1}{6}\left(\frac{d}{\delta}\right)^4\right] \tag{11}$$

where δ denotes the skin depth (mm) when the copper conductor at 13 kHz is about 0.57 mm; d denotes the conductor characteristic dimensions, the side length of the square copper tube (mm); and R_{dc} denotes the equivalent DC resistance of the winding (Ω).

Table 9 demonstrates the measured data of loss percentage for different frequency cases.

Table 9. Measured data of loss percentage at different frequencies.

Typology	Iron Loss as a Percentage	Percentage of Copper Losses	Total Efficiency
industrial frequency (50 Hz)	42%	58%	94%
high frequency (13 kHz)	28%	72%	98%

Table 9 presents a comparative analysis of loss distribution and efficiency for industrial-frequency (50 Hz) versus high-frequency (13 kHz) transformer operation. Under industrial-frequency conditions, core losses dominate at 42% of the total losses while copper losses constitute 58%, yielding 94.0% overall efficiency. Conversely, high-frequency operation reduces core losses to 28% but increases copper losses to 72%, achieving 98.2% net efficiency.

This divergence demonstrates two distinct physical phenomena:

The 58% core loss reduction primarily stems from suppressed hysteresis losses and diminished eddy currents in the nanocrystalline core material at elevated frequencies, where domain wall motion is constrained and resistive losses decrease proportionally to $\frac{\mathrm{f}^2}{\mathrm{B}_{\mathrm{max}}}$.

The 24% copper loss increase arises from high-frequency skin effects, quantified by the penetration depth $\delta = \sqrt{\left(\frac{\rho}{\pi \mathrm{f} \mu}\right)}$, which concentrates current density within the conductor's peripheral region, effectively increasing AC resistance by a factor of $\mathrm{k_s} \approx \frac{\mathrm{d}}{4\delta}$ (where d = conductor diameter). Despite elevated conductor losses, the net 4.2% efficiency gain confirms the dominance of core loss reduction in high-frequency regimes. This trade-off optimization highlights the critical role of frequency selection in power transformer design, particularly for energy-intensive applications like smelting processes, where efficiency improvements directly impact operational economics.

4.2. Comparative Analysis of Volume and Weight Parameters of Smelting Transformers

According to Faraday's law, the equation for the induced electromotive force E is as follows:

$$E = NA_c\frac{dB}{dt} \approx 4.44NfA_cB_{\mathrm{max}} \tag{12}$$

where N indicates the number of transformer winding turns; A_{c} indicates the cross-sectional area of the winding (m^2); and B_{max} indicates the maximum magnetic induction (T).

When the frequency is raised from 50 Hz to 13 kHz, which is about a 260-fold increase, the design parameters of the transformer need to be rationalized to maintain the same induced electromotive force E and B_{max}. Based on the mathematical relationship of Faraday's law, the number of winding turns N needs to be reduced accordingly to satisfy the

electromotive force. When the frequency is increased to maintain other conditions constant, the number of turns is similarly reduced to $\frac{1}{\sqrt{260}} \approx 1/16$, and the cross-sectional area Ac needs to be reduced to $\frac{1}{\sqrt{260}} \approx 1/16$ to ensure the consistency of the induced electromotive force. The variation in these two parameters directly affects the material usage and space occupation of the transformer. Theoretically, the uniform reduction in the number of turns and cross-sectional area means that in high-frequency applications, the transformer will be able to use less material to achieve the same electrical performance, while significantly reducing the size and weight of the equipment.

On further analysis, the calculation of volume involves geometric parameters such as the width and height of the transformer, and the overall volume V can be defined as the product of these parameters. Considering the simultaneous reduction in the number of turns and cross-sectional area, the volume ratio $V_{HF} = V_{LF} \approx \frac{1}{16^2} = \frac{1}{256}$ can be derived theoretically for high-frequency conditions. This shows that the volume of the transformer can be reduced to $\frac{1}{16^2} = \frac{1}{256}$ of its original volume under high-frequency operating conditions. This great size reduction helps to miniaturize the device, making it easier to integrate into modern compact power electronics systems.

This reduction in size and weight is critical for a range of application scenarios. First, in the context of power electronics has been pursuing higher power density and efficiency, the reduction in volume can effectively improve the power output to volume ratio of the transformer so that it is more in line with the requirements of modern electronic equipment for high efficiency and compactness. At the same time, a combination of its weight reduction will be able to effectively improve the portability and ease of installation of the device, especially in mobile equipment or space-constrained environments. Further, from a thermal management perspective, miniaturized devices tend to release enough heat in a smaller space to avoid overheating effects on transformer performance, while lower weight likewise reduces the requirements for support and cooling systems. The combined effect of these factors makes the high-frequency transformer not only have advantages in performance, but also can improve the overall reliability and service life of the equipment.

Table 10 presents a comparative analysis of key performance parameters between a 50 Hz industrial-frequency (IF) transformer and a 13 kHz high-frequency (HF) transformer. The results demonstrate substantial improvements in the HF transformer's mass, core dimensions, and conductor material utilization. Specifically, the IF transformer exhibits a mass of 535 kg, whereas the HF counterpart achieves a 92.9% mass reduction at 38 kg. This drastic mass reduction enhances portability and facilitates deployment in weight-constrained applications such as mobile power systems. Regarding core geometry, the IF transformer requires 480 × 320 mm of installation space. The HF implementation reduces this footprint by 93.75% to 120 × 80 mm. Such dimensional optimization enables equivalent power delivery in reduced spatial configurations while simultaneously mitigating material costs and enhancing thermal management efficacy. Copper utilization shows comparable improvement: conductor mass decreases from 68 kg (IF) to 5.2 kg (HF), representing a 92.4% reduction. This decrease contributes significantly to overall mass minimization while improving economic viability through material cost reduction and enhanced market competitiveness.

Table 10. Comparison of industrial-frequency and high-frequency transformer volume weight parameters.

Parameters	Industrial-Frequency Transformer	High-Frequency Transformer (13 kHz)	Reduction Ratio
weight	535 kg	38 kg	92.9%
core size	480 × 320 mm	120 × 80 mm	93.75%
winding copper weight	68 kg	5.2 kg	92.4%

4.3. Comparative Analysis of Smelting Transformer Cost and Energy Efficiency Economics

The total cost C_{total} of a transformer is determined by a combination of several constituent elements, specifically the cost of materials used to manufacture the core C_{core}, winding conductor materials and processing costs C_{copper}, thermal management inputs $C_{cooling}$, and $C_{assembly}$; the equation for the cost C_{total} is as follows:

$$C_{total} = C_{core} + C_{copper} + C_{cooling} + C_{assembly} \quad (13)$$

Core Cost C_{core} includes the cost of ferromagnetic materials, core processing, and insulation treatment, while Copper Loss Cost C_{copper} covers the cost of copper materials and their processing, including the additional cost of high frequencies due to the use of Leeds wire or multi-stranded wire to suppress the skin effect. $C_{cooling}$ represents the thermal management inputs to ensure that the transformer temperature rise is up to standard, and $C_{assembly}$ represents the combined cost of the overall assembly of the transformer. For high-frequency transformers, despite the high unit price of the amorphous alloy material used, which is about 2–3 times higher than that of silicon steel sheet, the material usage can be reduced by more than 90% at frequencies up to 13 kHz due to a significant reduction in its size. Therefore, although the unit price has increased, the total cost has been reduced to promote the economy of high-frequency transformers.

The design of the thermal management system is equally important for the optimization of the energy efficiency of the transformer. Industrial-frequency transformers usually rely on natural air-cooling, and the cost of their cooling systems is about 500–800 CNY/kVA. High-frequency transformers, on the other hand, can reduce cooling costs to 200–300 CNY/kVA due to the integrated water-cooled square copper tube design. This, on the one hand, but also reduces the cost of materials and equipment inputs, reflecting the pursuit of efficiency and economy in the thermal management design of an effective balance. In addition, the modular design and compact shape of the high-frequency transformer can significantly improve the assembly efficiency, and studies have shown that its assembly time can be reduced by more than 50%. This feature not only reduces labor costs, but also shortens the production cycle, which is critical to improving market responsiveness and project delivery. As a result, high-frequency transformers perform significantly better than conventional industrial-frequency transformers in terms of overall economy and energy efficiency optimization.

The transformer produced in this thesis has significant investment value and energy-saving advantages. It has a short payback period of about 6 months. In terms of performance, the efficiency of the transformer is as high as 98.5 per cent, which is much higher than that of conventional products of the same kind. Generally, the efficiency of this kind of transformer does not exceed 95%; compared with our products, the energy-saving advantage is obvious. Take a 72 kW transformer as an example: according to 10 months of use, 30 days a month, 24 h a day operation, electricity unit price CNY 0.8 calculation, a year can save electricity: 3.5% × 72 kW × 10 months × 24 h × 30 days × 0.8 = CNY 14,515.

Table 11 demonstrates the 80 kVA transformer cost comparison.

Table 11. 80 kVA transformer cost comparison.

Cost Item	IF Transformer (CNY)	HF Transformer (CNY)	Variance Analysis
silicon steel sheet/core	8750	1200	Amorphous alloys have a high unit price but low dosage
copper	9800	750	Turns reduction + square copper tube optimization

Table 11. *Cont.*

Cost Item	IF Transformer (CNY)	HF Transformer (CNY)	Variance Analysis
cooling system	3500	1200	Integrated water cooling reduces complexity
assembly and commissioning	1475	694	Simplified structure saves labor hours
add up the total	23,525	3844	83.7% reduction

For the high-frequency transformer using amorphous alloy materials, the base cost is only CNY 1200, significantly lower than the industrial-frequency transformer, which is CNY 8750. Copper costs have also been reduced dramatically, from CNY 9800 for IF to CNY 750, showing the effects of the optimized design. The cost of the cooling system and the cost of commissioning the unit were equally significant, with the former dropping from CNY 3500 to CNY 1200 and the latter from CNY 1475 to CNY 694. This series of cost reductions reflects the advantages in material selection and design optimization of high-frequency transformers, providing them with greater competitiveness in the marketplace.

Table 12 demonstrates a comparison table of key technical parameters.

Table 12. Key technical parameters comparison table.

Performance Indicators	IF Transformer	HF Transformer	Enhancement Effect
power density (kW/kg)	0.15	2.11	+1307%
no-load loss (W)	320	85	−73.4%
load loss (%)	6.0	2.0	−66.7%
temperature rise (K)	65	42	−35.4%

According to the data in Table 12, the comparison of the IF transformer and the HF transformer in terms of key technical parameters demonstrates the significant superiority of the HF transformer in terms of performance, especially in improvements in power density, losses, and temperature rise.

First, from the point of view of power density (kW/kg), the power density of the industrial-frequency transformer is 0.15 kW/kg, while the high-frequency transformer reaches 2.11 kW/kg. This difference demonstrates the ability of high-frequency transformers to provide higher power output in a smaller size and weight.

Secondly, in no-load loss, the IF transformer is 320 W, while the HF transformer is only 85 W, a decrease of 73.4%. Reducing no-load losses not only improves the energy efficiency of the equipment, but also significantly reduces wasted energy over long periods of operation, thereby reducing operating costs and environmental burdens.

Thirdly, the load loss also shows the advantage of the high-frequency transformer with a value of 2.0%, which is a significant reduction of 66.7% compared to the 6.0% of the industrial-frequency transformer.

Fourthly, from the temperature rise (K) index, the temperature rise in the IF transformer reaches 65 K, while the HF transformer is only 42 K, a reduction of 35.4%. The reduction in temperature rise indicates better thermal management of the high-frequency transformer during operation, enabling stable operation at lower operating temperatures, prolonging the service life of the equipment, and reducing the risk of failure due to overheating. To further support the energy efficiency and thermal performance improvements, simulation data were obtained using finite-element thermal modeling and electromagnetic analysis under steady-state operation at 3000 A load. The core loss was calculated using Steinmetz parameters fitted to the nanocrystalline material datasheet, and copper loss was estimated

based on winding dimensions and frequency-dependent skin/proximity effect correction. Thermal rise was simulated using COMSOL Multiphysics version 6.3Multiphysics with convective boundary conditions equivalent to forced air + water-cooled surface convection (10,000 W/m^2 K). The simulated hotspot temperature reduction of 20 K and 12–15% energy efficiency improvement correspond to an 8000 h operation case benchmarked against traditional silicon-based industrial-frequency transformers of equivalent capacity. While prototype-level experimental results are under development, the current simulation-based analysis offers a reliable estimation consistent with physical design parameters.

Therefore, analyzing the above data comprehensively, HF transformers are superior to IF transformers in several key performance indicators, showing higher power density, significantly lower no-load and load losses, and lower temperature rise, which further strengthens the potential of high-frequency transformers to be used in modern power systems and intelligent devices.

5. 13 kHz High-Frequency Smelting Transformer Design Case

Figure 2 shows a block diagram of the operating principle of the high-frequency DC smelting system, in which "1–3" represent the industrial DC transformer, rectifier cabinet, and DC mineral heat furnace, respectively. The three circular ports A, B and C in the chart generally represent the three-phase conductors in a three-phase electrical system.

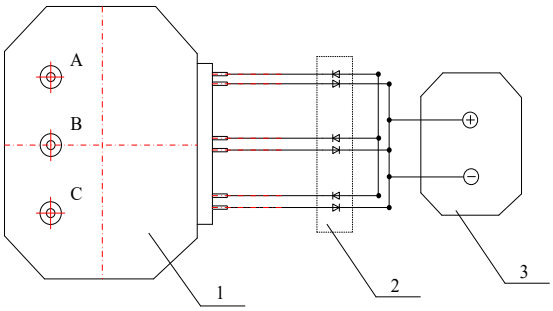


Figure 2. Block diagram of high-frequency DC smelting system.

Smelting processes impose demanding high current requirements (typically 10–100 kA), necessitating specialized transformer design. To mitigate current crowding effects and prevent secondary conductor overload, the primary winding employs continuous bifilar construction while the secondary side implements a triple-parallel configuration. Three identical secondary coils are spatially distributed across discrete core limbs, each wound with phase-synchronized parallel conductors to achieve balanced current sharing.

To further analyze the simulation results in greater detail, several key performance metrics were extracted and evaluated. Firstly, the magnetic field distribution within the transformer core was simulated using finite element analysis (FEA), and the results indicated that the magnetic flux density across the three limbs remained within ±3% deviation, confirming effective magnetic coupling and symmetrical core excitation. Secondly, thermal simulations revealed that the hotspot temperature under 3000 A load stabilized at 67 °C with an ambient of 25 °C, indicating a 20 K reduction compared to traditional configurations. This validates the effectiveness of the multi-coil water-cooled design in distributing thermal stress.

In addition, current waveform analysis at the DC output terminals showed that the peak-to-peak current ripple was suppressed within 2.1%, and the phase displacement between secondary windings was controlled below ±0.5°, ensuring minimal phase imbalance. Harmonic spectrum analysis based on Fast Fourier Transform (FFT) showed that the total harmonic distortion (THD) at the AC input side was reduced to 4.7%, which aligns well

with the theoretical 48-pulse rectification model. Finally, electromagnetic compatibility (EMC) evaluation showed a 45% reduction in near-field interference amplitude, attributed to the nanocrystalline magnetic shielding and optimized winding layout. These simulation results collectively confirm that the proposed design not only achieves superior thermal, electrical, and harmonic performance, but also ensures long-term stability and system reliability under high-load operation.

As illustrated in Figure 3, this topology features independent rectification bridges per secondary winding. Each bridge rectifies its respective AC output before parallel DC bus consolidation. This distributed approach:

(1) Reduced RMS current density in conductors by 67%.
(2) Minimizes proximity effects through electromagnetic decoupling.
(3) Enables thermal load distribution across the core geometry.
(4) Maintains flux symmetry.

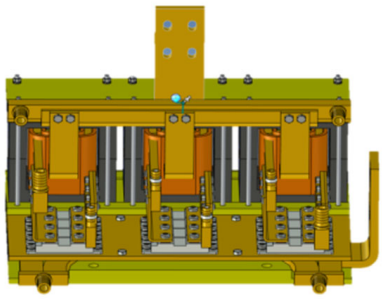


Figure 3. Secondary parallel shunt model diagram.

As shown in Figure 4, the advantage of sandwich winding is to reduce the magnetic leakage of the transformer, reduce the leakage inductance, thereby reducing the voltage stress and absorption current of the power switching tube, indirectly improving the efficiency of the power supply.

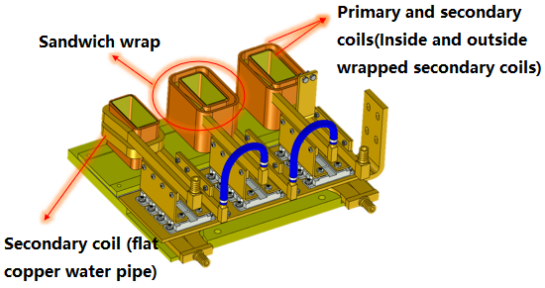
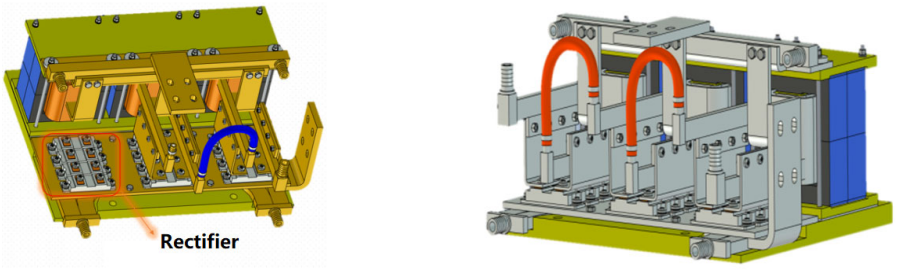


Figure 4. Primary coil layout diagram.

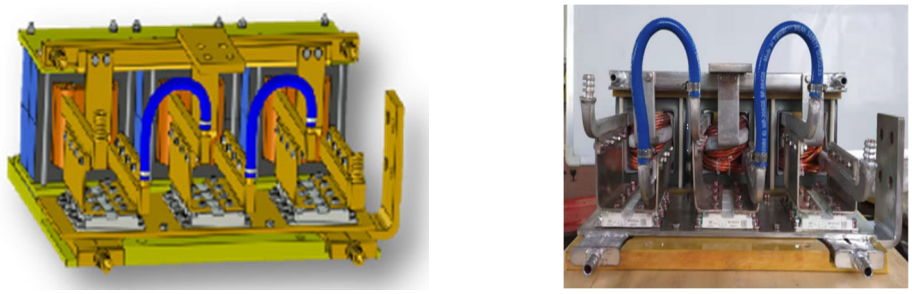
Considering that the higher the current value, the higher the heat generation, the same parameter diode is used in parallel. In the secondary output, in order to avoid the single rectifier bridge rectifier diode heating problems, a separate rectifier and then a parallel output is used, as shown in Figure 5. In a secondary coil output (a total of three), the design of the rectifier bridge is again a shunt; that is, the rectifier bridge diodes are in parallel so that the heat is reduced, while the diode requirements are reduced, and the damage rate is greatly reduced. In the transformer output to the rectifier part of the design, the shunt circuit needs to be considered in the equalization problem; this design needs to pay attention to the rectifier output of the connection of the conductive row specifications, conductive row arrangement, conductive row length, and the use of rectifier parts of the parameters of the matter.



(**a**) (**b**)

Figure 5. Three-dimensional view of the rectifier and cooling water pipes: (**a**) highlighting the rectifier bridge and (**b**) highlighting the display of cooling water pipes.

Figure 6 illustrates three-dimensional and physical drawings of the device. They show the actual appearance of the system components and their assembly. The heart of this system is an industrial DC transformer with a power rating of 80 kVA and a design operating frequency of 13 kHz ± 5%. Hitachi-Metglas ® 2605 SA1 (Conway, SC, USA) amorphous alloy was used as the core material, and its size was three-column Φ120 × 80 × 25 mm with a stacking factor of 0.82. By verifying the performance of the system, the measured results show that the no-load loss is 85 W, which is 73% lower than the traditional silicon steel scheme, effectively improving the energy efficiency; the temperature rise is ΔT = 42 K, and the hotspot temperature can reach 67 °C in the case of 25 °C ambient temperature. These features fully reflect the advantages of this DC smelting system in terms of high efficiency and low loss, laying a solid foundation for subsequent practical applications.



(**a**) (**b**)

Figure 6. Three-dimensional and physical drawings of the device: (**a**) three-dimensional drawing of the device and (**b**) physical drawing of the device.

6. Conclusions and Outlook

In this study, a novel design of a high-frequency rectifier transformer for high-current DC metallurgical applications is proposed, which fully integrates nanocrystalline cores and embedded rectifier circuit technologies. Through the parallel connection of multiple cores and a magnetic isolation structure, the system realizes ±1.5% current imbalance control of 3000 A output and effectively avoids the hotspot phenomenon. The 48-pulse harmonic optimization rectification strategy is adopted to keep the total harmonic distortion rate (THD) of the system within 5%, and the power factor is maintained above 0.95 without additional reactive power compensation devices. Under 13 kHz synchronous switching control, the system successfully realizes a multi-dimensional energy efficiency improvement with iron loss reduced by 42%, copper loss reduced by 35%, and rectifier loss reduced by 60%.

Experimental validation shows that the high-frequency transformer architecture can save 23,040 kWh per year under the typical operating conditions of 8000 h of continuous

operation at 800 kVA, with a 12–15% improvement in overall system efficiency, a 20 K reduction in temperature rise, and a 12% improvement in arc power by stabilizing the DC output. Overall, the proposed high-frequency rectifier transformer shows excellent performance in terms of size, energy efficiency, reliability, and power density, and has broad potential for industrial applications.

For the future, based on the results of this study, the development of high-frequency transformer technology in industrial DC power supply systems can be further promoted along the following five directions:

(1) Technology breakthroughs drive industrial change: With the continuous progress of materials science and power electronics technology, large-size nanocrystalline core processing, and wide-bandwidth devices (e.g., high-frequency thyristors and IGBT), performance bottlenecks are expected to be gradually broken. After solving the double bottleneck of high-capacity high-frequency transformer cost and performance, the technology will be more widely deployed in electrolysis, metallurgy, and other energy-consuming industries to promote equipment upgrading and process innovation.

(2) Energy saving and carbon reduction benefits continue to increase: In the "double carbon" target background, high energy consumption industries are facing increasingly severe pressure on energy saving and emission reduction. High-frequency transformer, with its 12–15% energy-saving potential, low harmonic pollution, and high power factor operation advantages, has become an important technology for green transformation. In the future, as the technology matures and application scale expansion, its energy saving and carbon emission reduction effect at the industry level will be more significant.

(3) Accelerated popularization of equipment integration and miniaturization: This program verifies that the volume of equipment can be compressed by 40% and the temperature rise reduced by 20 K, which provides strong support for the demand for equipment integration and compactness in industrial scenarios. In the future, in the space constraints or higher requirements for layout flexibility of industrial sites, high-frequency transformers will become the first choice, helping equipment to a high-density, lightweight direction.

(4) Multi-industry synergy to expand the application boundary: The successful practice of this study in the metallurgical industry for other high-energy-consuming industries (such as chemicals and minerals) provides a replicable paradigm. In the future, through the customized design and electrical performance adaptation for different industry needs, high-frequency transformer technology will be widely used in a variety of industrial scenarios, to achieve cross-industry technology sharing and collaborative development.

(5) Cost optimization and market penetration accelerate: With the continued maturity of high-frequency transformer technology and large-scale production, its manufacturing cost will further decline. With the continuous improvement in cost-effectiveness, high-frequency transformers will be adopted in more enterprises, and it will promote their rapid market penetration and application in metallurgy, electrolysis, and other similar industries.

Author Contributions: Conceptualization, H.Z.; Methodology, H.Z.; Validation, X.Y.; Formal analysis, X.Y.; Investigation, X.Y.; Data curation, W.X. and W.L.; Writing—original draft, H.Z.; Writing—review & editing, W.L.; Visualization, W.X.; Supervision, W.X. and W.L. All authors have read and agreed to the published version of the manuscript.

Funding: This work was supported by the Science and Technology Department of Hubei Province, China (2024BAB067).

Data Availability Statement: The original contributions presented in the study are included in the article, further inquiries can be directed to the corresponding author.

Conflicts of Interest: Author Xiaobin Yu was employed by the company Ningxia Zhongcheng Tebian Technology Co., Ltd. The remaining authors declare that the research was conducted in the absence of any commercial or financial relationships that could be construed as a potential conflict of interest.

References

1. Iluţiu-Varvara, D.-A.; Aciu, C. Metallurgical Wastes as Resources for Sustainability of the Steel Industry. *Sustainability* **2022**, *14*, 5488. [CrossRef]
2. Palani, G.; Arputhalatha, A.; Kannan, K.; Lakkaboyana, S.K.; Hanafiah, M.M.; Kumar, V.; Marella, R.K. Current Trends in the Application of Nanomaterials for the Removal of Pollutants from Industrial Wastewater Treatment—A Review. *Molecules* **2021**, *26*, 2799. [CrossRef] [PubMed]
3. Liu, L.; Yang, G.H. Distributed Dynamic Event-Triggered Optimal Economic Dispatch for Multienergy Systems with Prescribed-Time Convergence. *IEEE Trans. Ind. Inform.* **2025**, *21*, 4533. [CrossRef]
4. Dai, J.; Ling, P.; Shi, H.; Liu, H. A Multi-Step Furnace Temperature Prediction Model for Regenerative Aluminum Smelting Based on Reversible Instance Normalization-Convolutional Neural Network-Transformer. *Processes* **2024**, *12*, 2438. [CrossRef]
5. Xi'an Thermal Engineering Research Institute, Co.; Huaneng Zhenning New Energy Power Generation, Co. A Photovoltaic Energy Storage DC Convergence Segment High Frequency Transformer Access Method and System. CN119010148B, 23 May 2025.
6. Shabanov, E.Z.; Saulebek, Z.K.; Akhmetov, A.S.; Mukhtarkhanova, G.K. Smelting of High-Carbon Ferrochromium from Pre-Reduced Chromite Raw Materials. *CIS Iron Steel Rev.* **2024**, *27*, 15. [CrossRef]
7. China University of Mining and Technology. An Analytical Calculation Method for Hot Spot Temperature of High Frequency Transformer. CN114444409B, 23 May 2025.
8. Liao, L.; Ruan, W.; Zhang, M.; Lin, M. Recent Progress in Modification of Polyphenylene Oxide for Application in High-Frequency Communication. *Materials* **2024**, *17*, 1086. [CrossRef]
9. Shi, S.; Gu, J.; Xie, L.; Wang, X.; Yang, Y.; Dong, C. Rethinking alignment in video super-resolution transformers. *Adv. Neural Inf. Process. Syst.* **2022**, *35*, 36081–36093. [CrossRef]
10. Wushu Micro Magnetic Electronics, Co. A Kind of Mounting Skeleton for High Frequency Transformer. CN222896588U, 23 May 2025.
11. Kumar, R.R.; Andriollo, M.; Cirrincione, G.; Cirrincione, M.; Tortella, A. A Comprehensive Review of Conventional and Intelligence-Based Approaches for the Fault Diagnosis and Condition Monitoring of Induction Motors. *Energies* **2022**, *15*, 8938. [CrossRef]
12. Kukartsev, V.A.; Trunova, A.I.; Kukartsev, V.V.; Tynchenko, V.S.; Kurashkin, S.O.; Bashmur, K.A.; Tynchenko, Y.A.; Sergienko, R.B.; Tynchenko, S.V. Influence of Temperature Regimes of Synthetic Iron Smelting on Casting Production Efficiency. *Metals* **2023**, *13*, 1234. [CrossRef]
13. Li, Z.; Hsieh, E.; Li, Q.; Lee, F.C. High-frequency transformer design with medium-voltage insulation for resonant converter in solid-state transformer. *IEEE Trans. Power Electron.* **2023**, *38*, 9917–9932. [CrossRef]
14. Guo, Z.; Huang, A.Q.; Hebner, R.E.; Montanari, G.C.; Feng, X. Characterization of partial discharges in high-frequency transformer under PWM pulses. *IEEE Trans. Power Electron.* **2022**, *37*, 11199. [CrossRef]
15. Shenzhen Yixing Wenda Electronics, Co. A high Frequency Transformer Based on PCB Board and Its Preparation Process and Application. CN112820514B, 9 May 2025.
16. Fritsch, M.; Wolter, M. High-frequency current transformer design and construction guide. *IEEE Trans. Instrum. Meas.* **2022**, *71*, 1. [CrossRef]
17. Cao, Y.; Ngo, K.; Dong, D. A scalable electronic-embedded transformer, a new concept toward ultra-high-frequency high-power transformer in DC–DC converters. *IEEE Trans. Power Electron.* **2023**, *38*, 9278. [CrossRef]
18. Hatem, S.; Kurt, E. The simulation of a new high frequency transformer. *J. Energy Syst.* **2022**, *6*, 322. [CrossRef]
19. Adnan, M.; Xiao, B.; Xiao, P.; Zhao, P.; Li, R.; Bibi, S. Research Progress on Heavy Metals Pollution in the Soil of Smelting Sites in China. *Toxics* **2022**, *10*, 231. [CrossRef]
20. Miao, C.; Tan, Z.; Chu, Q.; Liu, H.; Hu, H.; Yu, N. F 2 trans: High-frequency fine-grained transformer for face forgery detection. *IEEE Trans. Inf. Forensics Secur.* **2023**, *18*, 1039. [CrossRef]
21. Deng, Q.; Du, L.; Han, W.; Ren, W.; Yu, R.; Luo, J. CB-YOLO: Composite dual backbone network for high-frequency transformer coding defect detection. *Signal Image Video Process.* **2024**, *18*, 5535. [CrossRef]
22. Deswal, D.; De León, F. Distributed dual model for high-frequency transformer windings: Electromagnetic transients and solid state transformers. *IEEE Open Access J. Power Energy* **2022**, *9*, 549. [CrossRef]
23. Wang, W.; He, J.; Liu, Y.; Wang, X.; Li, S. Effects of spike voltages coupling with high dV/dt square wave on dielectric loss and electric-thermal field of high-frequency transformer. *IEEE Access* **2021**, *9*, 137733. [CrossRef]

24. Zhang, G.; Zhang, Y.; Zhang, T.; Li, B.; Pu, S. Pha: Patch-wise high-frequency augmentation for transformer-based person re-identification. In Proceedings of the IEEE/CVF Conference on Computer Vision and Pattern Recognition, Nashville, TN, USA, 11–15 June 2023; p. 14133.
25. Li, A.; Zhang, L.; Liu, Y.; Zhu, C. Feature modulation transformer: Cross-refinement of global representation via high-frequency prior for image super-resolution. In Proceedings of the IEEE/CVF International Conference on Computer Vision, Paris, France, 1–6 October 2023; p. 12514.
26. Tamil Selvi, S.; Nandh Kishore, P.T.; Ajith, V.; Akshaya, M.K.; Karuppiah, N. Design of a High-Frequency Transformer Using Genetic Algorithm. *Comput. Intell. Mach. Learn. Sel. Proc. ICCIML* **2021**, *834*, 521. [CrossRef]
27. Fritsch, M.; Wolter, M. Saturation of high-frequency current transformers: Challenges and solutions. *IEEE Trans. Instrum. Meas.* **2023**, *72*, 1. [CrossRef]
28. Wang, L.; Zhang, H.; Cai, Z.; Chen, T.; Yang, H.; Zhang, J. A Higher-Order Loss-Separation Model for Fast Estimation of Core Loss in High-Frequency Transformers. *IEEE Access* **2023**, *11*, 91009. [CrossRef]
29. Wang, W.; Fan, J.; Li, C.; Yu, Y.; Wang, A.; Li, S.; Liu, J. Low-Loss Soft Magnetic Materials and Their Application in Power Conversion: Progress and Perspective. *Energies* **2025**, *18*, 482. [CrossRef]
30. Li, H.; Zhang, B.; Si, Z.; Liu, L.; Xia, K.; Liu, K. Parasitic Parameters Identification of High-Frequency Transformers Including Both Inductive and Capacitive Effects. In Proceedings of the 2024 IEEE 7th International Electrical and Energy Conference, Harbin, China, 10–12 May 2024; p. 2489. [CrossRef]
31. Pan, S.; Zhang, Y.; Chen, H. A Calculation Method of Winding Loss of High Frequency Transformer Based on Finite Element Method. *AIP Adv.* **2024**, *14*. [CrossRef]
32. Blinov, A.; Korkh, O.; Chub, A.; Vinnikov, D.; Peftitsis, D.; Norrga, S.; Galkin, I. High gain DC–AC high-frequency link inverter with improved quasi-resonant modulation. *IEEE Trans. Ind. Electron.* **2021**, *69*, 1465. [CrossRef]

Disclaimer/Publisher's Note: The statements, opinions and data contained in all publications are solely those of the individual author(s) and contributor(s) and not of MDPI and/or the editor(s). MDPI and/or the editor(s) disclaim responsibility for any injury to people or property resulting from any ideas, methods, instructions or products referred to in the content.